Corrosion Monitoring and Assessment of Steel under Impact Loads Using Discrete and Distributed Fiber Optic Sensors

Luyang Xu ¹, Shuomang Shi ¹, Ying Huang ^{1*}, Fei Yan¹, Xinyi Yang¹, and Yi Bao ²

¹ Department of Civil, Construction, and Environmental Engineering, North Dakota State University, Fargo 58102

² Department of Civil, Environmental and Ocean Engineering, Stevens Institute of Technology, Hoboken, New Jersey 07030

* Corresponding author: ying.huang@ndsu.edu

Abstract

Structural integrity can be compromised by the simultaneous presence of mechanical loads and corrosive agents. This study investigates the complex interplay between corrosion and impact loads in steel plates, utilizing discrete Fiber Bragg Grating (FBG) and distributed Optical Frequency Domain Reflectometry (OFDR) sensing technology. Generalized fiber optic-based sensing models are developed to quantify corrosion severity and rate. The experimental study was conducted using twelve epoxy-coated steel plates equipped with FBG and OFDR sensors, covering scenarios of individual exposure to corrosion, impact loads, as well as their combination. Test results reveal that specimens subjected to combined conditioning exhibit more corrosion damage than those subjected to individual corrosion. Both pit depth and its growth rate were exacerbated due to the impact loads. The study demonstrates the potential of fiber optic sensors (FOSs) for real-time monitoring and assessment of structural health under different simultaneous multiple factors in challenging conditions.

Keywords: Corrosion, Impact loads, Fiber Bragg Grating (FBG), Optical Domain Reflectometry
 (OFDR), Pit Depth, Fiber Optic Sensors (FOSs).

1. Introduction

Corrosion is one of the most significant factors contributing to the degradation of aging infrastructures, including buildings, highway bridges, oil and gas transmission pipelines, and railroads [1]. It casts a pervasive shadow over both their structural integrity and operational reliability, and further leads to a substantial economic burden due to frequent repairs and rehabilitations [2]. Thus, optimal corrosion monitoring and assessment practices need to be conducted in order to maintain and extend the designed lifetime of these aging infrastructures.

Corrosion of structural steel is a natural electrochemical reaction resulting in rust formation when exposed to moisture and oxygen. It manifests in various forms of deterioration on metallic substrates [3, 4]. Among these, uniform and localized corrosion stand out prominently, each characterized by distinct mechanisms and consequences, as depicted in Fig. 1. Uniform corrosion involves a relatively even loss of material across the surface, while localized corrosion induces concentrated yet potentially severe damage. Corrosion control strategies typically incorporate physical barriers, such as various coatings, to isolate the metal substrate from the surrounding electrolyte layer. However, coating defects and anomalies can permit water uptake from the environment, leading to the formation of corrosion products and influencing corrosion kinetics. Specifically, pitting corrosion, a form of localized corrosion, can cause profound degradation of

the steel substrate. Small pits initially have the potential to expand and merge, resulting in significant defects in both depth and length, as shown in Fig. 1 [5]. In the marine environment, the typical ionic compound, sodium chloride (NaCl), is regarded as a strong electrolyte. It can dissolve in water to form Na⁺ and Cl⁻ ions [6]. Increasing the concentration of Cl⁻ ions in water results in a corresponding rise in current density. This increase is directly associated with the acceleration of the corrosion process, as it correlates with the rate of electrochemical reactions [7]. Furthermore, the presence of oxygen, an essential element for the cathodic phase of metallic corrosion in aqueous environments, has a significant impact on the redox reactions that occur throughout the corrosion process [8].

42

43

44

45

46

47

48

49

50

5152

53

54

55

56

5758

59

60

61

62

63

64

65

66 67

68

69

70

71

72

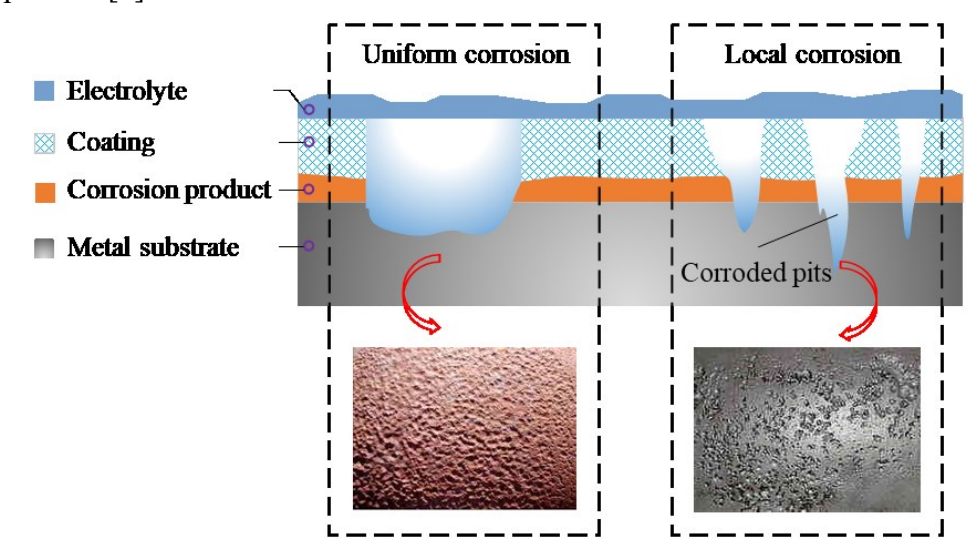


Fig. 1 Typical corrosion forms of steel elements.

On the other hand, structures in service conditions are usually under external loads, and their integrity can be compromised by mechano-chemical effects. Gao et al. [9] explored the corrosion behavior of weathering steel with a bainitic microstructure exposed to chloride-rich environments under varying elastic stresses. They observed that higher stresses significantly accelerated corrosion. Zhang et al. [10] investigated the influence of loading conditions on low-carbon, lowalloy steel corrosion in NaCl solution, noting a marked acceleration of corrosion under applied elastic stress, particularly in dynamic loading. Melchers et al. [11] studied corrosion in the shipping industry and found significant rust layer damage near or beyond steel's elastic limit under high tensile strain. Moreover, short-term tests revealed a 10-15% increase in corrosion rates for precorroded steel. Dai et al. [12] observed decreased impact resistance in corroded reinforced concrete beams, while Fang et al. [13] reported increased crack propagation in corroded concrete piers under lateral impact. Additionally, Feng et al. [14] highlighted how corrosion impairs the elastic recovery of circular hollow tubes exposed to impact loads. These studies collectively emphasize the detrimental impact of corrosion on structural performance, underscoring the importance of simultaneous corrosion and mechanical load evaluation for timely damage identification and effective mitigation against structural failures.

In recent years, various sensors have been developed in various fields, such as the biosensor for aquaculture, marine life, and healthcare applications [15, 16], human health monitoring [17, 18], fiber optic gyro (FOG) identifying the rotation rate [19], silicon optical sensors [20], chirped fiber Bragg grating (CFBG) sensors [21, 22], and optical fiber specklegram sensors [23].

Simultaneously, to enable accurate corrosion monitoring, especially for early detection and ongoing development, advanced non-destructive technologies, such as Fiber Optic Sensors (FOSs), have emerged as a promising tool for structural health monitoring. These sensors offer the potential for enhanced accuracy and real-time insights, characterized by their compact size, lightweight nature, immunity to electromagnetic interference, as well as the desired physical and chemical stability [24, 25]. FOSs can be categorized into discrete (point) and distributed sensors. Among them, Fiber Bragg Grating (FBG) sensors and Distributed Fiber Optic Sensors (DFOSs) are two prominent types [26]. FBG sensors leverage periodic refractive index variations within the fiber core to reflect specific light wavelengths, enabling strain, temperature, and other measurements. They have been utilized to detect and monitor corrosion of reinforcing bars in concrete [27-30], steel plate [31-33], prestressed structures [34], and steel bridges [35]. Clearly, discrete point sensors are better suited for measuring the level of corrosion at their respective locations, especially for monitoring pitting corrosion. To address the limitations of FBGs with localized corrosion, DFOSs extend the capability across larger spatial scales [36]. They can provide continuous monitoring of key parameters along the entire optical fiber length. Sun et al. [37] employed Brillouin Optical Time Domain Reflectometry (BOTDR) to examine reinforced concrete expansion due to steel bar corrosion. Mao at al. [38] utilized Brillouin Optical Time Domain Analysis (BOTDA) and FBG sensors to monitor concrete expansion and cracking. However, BOTDR and BOTDA have limited spatial resolutions. To achieve high spatial resolutions, Fan et al. [39] proposed using Optical Frequency Domain Reflectometry (OFDR) to monitor steel pipe corrosion, establishing a theoretical model for quantifying corrosion severity and enabling corrosion visualization and alerts. Notably, research on dynamic load and corrosion interaction monitoring, essential for assessing structural behavior of steel under combined corrosion and dynamic load conditions, is currently limited.

For the first time, this paper deploys discrete and distributed FOSs to investigate the behavior of steel under simultaneous effects of impact loads and corrosion conditions. A comprehensive strategy is introduced to evaluate the severity of corrosion and the structural responses of the steel under the influence of impact loads only, corrosion only, and combined corrosion and impact loads simultaneously. The tested steel was coated with epoxy since, in practice, soft coatings were commonly applied to mitigate corrosion. The FBG and OFDR sensors were embedded inside the epoxy coatings to monitor and assess the integrity of the steel under simultaneous corrosion and impact loads, enriching the understanding of the complex interaction between impact loads and corrosion.

2. Discrete and distributed fiber optic sensing

73

74

75

76

77

78

79

80

81

82

83

84

85

86

87

88

89 90

91

92

93

94

95

96

97

98

99

100

101

102

103

104

105

106

107

108

109

110

111

112113

The methodology proposed integrates strain changes captured by FBG and OFDR-based distributed sensors to evaluate corrosion-induced pit depth. This approach utilizes wavelength changes measured by these sensors to estimate deformations induced by pitting corrosion and external loads, providing a means to assess pit depth. Furthermore, corrosion rate (CR) was also estimated, leveraging the measured wavelength changes of the fiber optic sensors. This estimation offers insights into the corrosion dynamics, facilitating comprehensive corrosion monitoring under impact loads.

2.1 FBG sensing principle

FBGs are engineered with meticulous precision by exposing a single-mode optical fiber core to intense ultraviolet light, inducing a periodic refractive index modulation that constitutes the grating structure [38]. Fig. 2 shows the functional mechanism inherent in an optical fiber containing an FBG [40]. Upon introduction of a broadband light source into the grating structure, a discernible fraction of the incident light undergoes reflection contingent upon the achievement of constructive interference prerequisites. This eventuality substantiates the alignment of the incident light with the designated Bragg condition [32, 41].

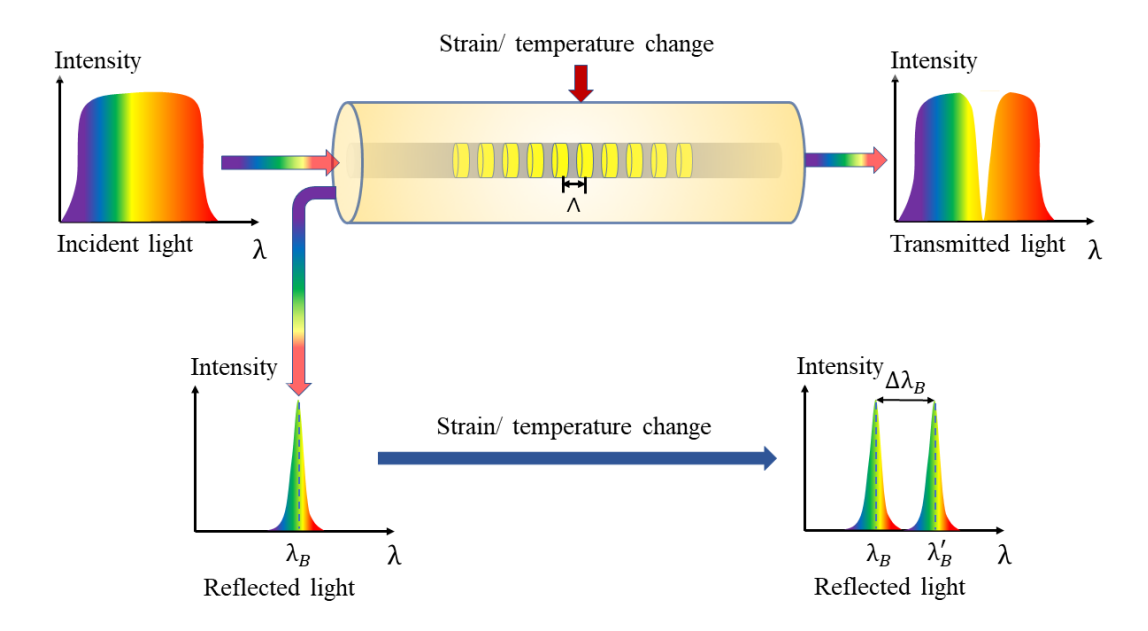


Fig. 2 FBG sensing principle.

Eq. (1) demonstrates the relationship between the Bragg wavelength (λ_B) and the grating parameters [40]:

$$\lambda_B = 2n_{eff} \,\Lambda \tag{1}$$

where n_{eff} is the effective refractive index; and Λ is the grating period corresponding to the distance between two adjacent grating planes. When subjected to temperature or strain changes, the constructive interference generated by the interaction between light and the grating period causes a shift in the Bragg wavelength ($\Delta\lambda_B$). This shift in the Bragg wavelength can be expressed in Eq. (2) [31, 42]:

$$\Delta \lambda_{R} = \lambda_{R} [(1 - P_{\rho}) \Delta \varepsilon + (\alpha + \xi) \Delta T]$$
 (2)

where λ_B is the Bragg wavelength; P_e is the photo elastic coefficient of the fiber; $\Delta \varepsilon$ is strain change; α and ξ are the respective thermal expansion coefficient and the thermos-optic coefficient of the fiber and are dependent on the material of fiber; and ΔT is the temperature change. If the temperature remains constant or is compensated by a strain-free reference sensor in identical operational conditions, the temperature influences could be eliminated [43]. Consequently, the strain change can be simplified as Eq. (3):

$$\Delta \varepsilon = \alpha \cdot \Delta \lambda_B \tag{3}$$

where $\alpha = \frac{1}{\lambda_B(1-P_e)}$. Clearly, the change in strain is converted into a change in Bragg wavelength.

When rust forms on the metal surface where the FBG sensor is located, it can be monitored and recorded in real-time. One of the major advantages of FBG sensors is their physical stability under dynamic loads. In addition, owing to the rapid data acquisition capability, FBG sensors are optimally configured for tracking dynamic phenomena and swift strain alterations. These sensors are efficient for measuring discrete points along the fiber but may require multiple sensors for distributed sensing, a topic that will be discussed in the next section.

2.2 OFDR-based distributed sensing principle

OFDR utilizes coherent light interference. A broadband optical source emits light guided through an optical fiber, interacting with its refractive index variations due to external factors like strain or temperature changes [44, 45]. Fig. 3 demonstrates the OFDR sensing principle. In Fig. 3 (a), for a given fiber, the scattering amplitude is a function of distance with unique, static, and highly repeatable properties along the fiber [46]. Temperature and strain induce shifts in the Rayleigh scattering spectrum, identified through cross-correlation between the reference and perturbed signals, as illustrated in Fig. 3 (b). Light excites Rayleigh scattering, and the amplitude of backscattered signals converts to the frequency domain via Fast Fourier Transform. The fiber divides into equally-length segments using a sliding window ΔX , allowing frequency shift evaluation through cross-correlation between reference and perturbed states.

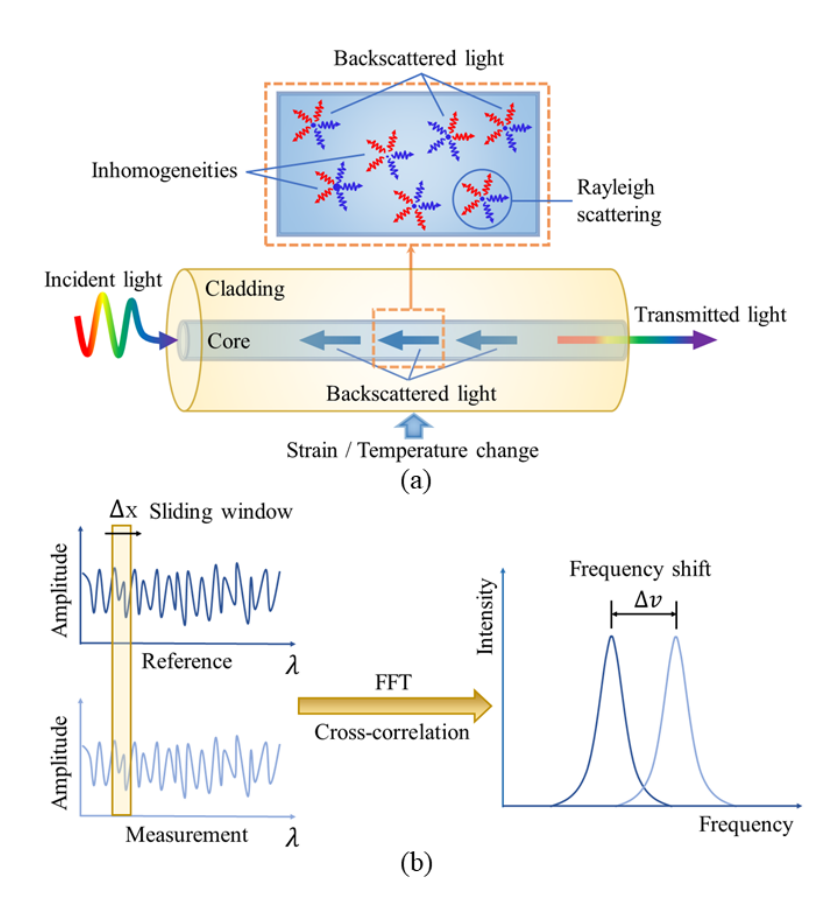


Fig. 3 OFDR sensing principle (a) a typical example of Rayleigh scattering in a single-mode optical fiber, and (b) signal processing principle for measuring strain or temperature changes in the OFDR system.

Eq. (4) illustrate the shift in optical wavelength in response to strain (ε) and temperature change (ΔT) [47]:

$$\Delta \lambda_D = \lambda_D \frac{\Delta v}{v} = \lambda_D (K_T \Delta T + K_\varepsilon \Delta \varepsilon) \tag{4}$$

where λ_D and v are the mean optical wavelength and frequency; K_T and K_ε are the temperature and strain calibration constants, which were calibrated as -0.15 and -1.46, respectively [39, 48]. When temperature remains stable, frequency shifts in the optical fiber are converted into strains using a calibrated strain sensitivity coefficient. Likewise, in cases of temperature fluctuations, a strain-free optical fiber can compensate for temperature variations. If the temperature remains constant or is compensated by a strain-free reference sensor in identical operational conditions, the temperature influences could be eliminated [39]. Consequently, the strain change can be simplified as Eq. (5):

$$\Delta \varepsilon = \beta \cdot \Delta \lambda_D \tag{5}$$

where $\beta = \frac{1}{\lambda_D K_E}$. Similar to FBG sensing principle, the change in strain is converted to the change in mean optical wavelength. OFDR-based sensing utilizes the interference patterns of frequency-swept light to provide high-resolution, distributed measurements along the entire length of the fiber. This allows for continuous monitoring with sub-millimeter spatial resolution, making it ideal for applications where fine-grained data is crucial, such as structural health monitoring and distributed temperature sensing. While FBG sensors are cost-effective and robust, OFDR offers unparalleled spatial precision and is particularly advantageous when detailed, continuous measurements are needed over a large area or along an extended fiber length. The choice between FBG and OFDR-based sensing depends on the specific requirements and constraints of the application at hand. Given the precedent of calibration procedures conducted in previous research [31, 39, 48] pertaining to FBG and OFDR-based distribute sensors, the current study still utilized the previous calibration standard. The specifications of the used FBG and OFDR sensors are illustrated in Table 1 provided by the manufacturer.

Table 1 Specifications of the FBG and OFDR-based fiber optic sensors.

| | Specification | | | | | | |
|--------------------------|-----------------------------------|-------------------------|--|--|--|--|--|
| Parameter | FBG | OFDR | | | | | |
| Strain measurement range | ±5,000 με | ±15,000 με | | | | | |
| Strain sensitivity | ~1.2 με/pm | ~1.0 με/pm | | | | | |
| Resolution | 0.1 με | 0.1 με | | | | | |
| Accuracy | $\pm 1.0~\mu \varepsilon$ | $\pm 1.0~\mu arepsilon$ | | | | | |
| Uncertainty | $\pm 0.04~\mu \varepsilon$ at 1Hz | ±2.0 με | | | | | |

2.3 Fiber optic-based sensing model for corrosion monitoring under impact loads

2.3.1 Pit depth estimation

The change in strain is evidently converted into a change in optical wavelength ($\Delta \lambda_B$ or $\Delta \lambda_D$), allowing fiber optic sensing technology to detect corrosion-induced strain in metals. Pitting corrosion often initiates due to minor scratches or coating damage on steel substrates, leading to the pitted area becoming anodic while the rest of the metal becomes cathodic, thus initiating a local electrochemical reaction. Pits typically manifest as cavities beneath the metal surface, acting as stress concentration sites [49]. This type of corrosion is highly localized, confined to specific, often concealed areas, and does not spread widely across the surface. Therefore, it is reasonable to assume that pits primarily develop vertically, allowing to model corrosion as an equivalent concentrated load applied to the corroded surface [31]. In the present study, corrosion products

remain on the substrate until they are removed. Consequently, pit-induced deformation can be captured in real-time by FOSs. Fig. 4 illustrates the simplified sensing model, depicting the deformations of the FOS under simultaneous corrosion and impact loading. In Fig. 4 (a), an equivalent upward force (F_c) from corrosion stretches the sensor, causing an upward displacement (Δ_c) due to corrosion protrusion. Conversely, in Fig. 4 (b), the external load (F_i) induces a downward bending deformation (Δ_i) . Thus, the synergistic effects of corrosion and external loads-induced stain changes in FOSs can be detected simultaneously.

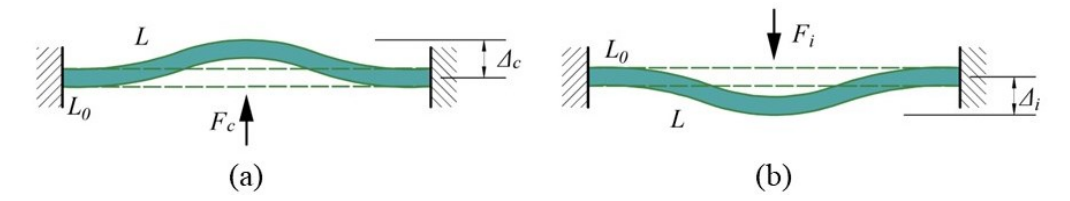


Fig. 4 Deformations of a beam model under (a) pitting corrosion, and (b) impact load.

The deformation of FOS ΔL both induced by corrosion and impact load can be approximated as:

$$\Delta L = L - L_0 \tag{6}$$

where L is the deformed length of the fiber optic sensor; and L_0 is the original length of the sensor.

Then, the strain in the FOS, $\Delta \varepsilon$, can be expressed as:

$$\Delta \varepsilon = \frac{\Delta L}{L_0} \tag{7}$$

For a triangular deformation, integrating Eq. (6), the combined displacement $\Delta = \Delta_c + \Delta_i$, can be estimated as:

$$\Delta = \frac{1}{2} \sqrt{L^2 - L_0^2} = \frac{1}{2} \sqrt{\Delta L \cdot (\Delta L + 2L_0)} = \frac{1}{2} L_0 \sqrt{\alpha \cdot \Delta \lambda_B (\alpha \cdot \Delta \lambda_B + 2)}$$
 (8)

Importantly, under impact loads, the load-induced elastic strain can return to zero within a few seconds after unloading, allowing to obtain $\Delta = \Delta_c$ for the combined corrosion and impact load conditioning. Integrating Eqs. (3) and (5) into Eq. (8), the corrosion-induced displacement using wavelength change of the FOSs can be calculated in the following:

For FBG sensors:

196

197

198

199

200

201

202

203

211

212213

214

215

$$\Delta_c = \frac{1}{2} L_0 \sqrt{\alpha \cdot \Delta \lambda_B (\alpha \cdot \Delta \lambda_B + 2)}$$
(9)

For OFDR-based DFOSs:

$$\Delta_c = \frac{1}{2} L_0 \sqrt{\beta \cdot \Delta \lambda_D (\beta \cdot \Delta \lambda_D + 2)}$$
 (10)

Thus, it is convenient to use Eqs. (9) and (10) to calculate the corrosion-induced displacements through the measurements of wavelength change of FBG and OFDR-based distributed sensors. Under epoxy coatings, corrosion usually occurs as pitting corrosion. As stipulated by ASTM-G46, pitting corrosion primarily manifests in two categories of shapes and geometries [50]. Trough pitting corrosion presents as small, elongated pits parallel to the surface, which can develop into channels or grooves. Alternatively, sidewall pitting corrosion forms depressions or craters on vertical or inclined surfaces of a substrate. The deceptive nature of surface pit openings as an indicator of sub-surface corrosion poses challenges in accurately assessing structural conditions. Pit depth modeling can be simplified to a two-dimensional (2D) problem, focusing on the penetration that threatens structural integrity by perforating steel substrates. Particularly for coated substrates, pitting corrosion occurs beneath the coatings, allowing the ingress of environmental agents. In our previous work [40], a generalized shape model is proposed to facilitate pit depth estimation during corrosion assessment. This model captures geometric characteristics of various pit shapes and represents most cases. The pit depth d is expressed as:

$$d = \frac{1.2\Delta_c}{c - 1} \tag{11}$$

where c is the volume ratio, which equals to the volume of the corrosion product above the steel surface divided by the volume of original steel [40]. Corrosion accumulates, concealing the indentations caused by pitting corrosion and generating raised areas on the steel surface. Typically, in standard conditions, the diameter of these elevated sections is approximately 10% to 20% greater than that of the initial inner cavity, $A_c = 1.1 \sim 1.2 A_0$ [51]. The volume with different constituents is usually different compared to the original iron α - F_e , and thus the volume ratio c is summarized in Table 2 [52]. It indicates that the volume of corrosion product can expand to 1.5-6 times the volume of the original iron.

Table 2 Volume ratio c of corrosion product with different constituents [52].

| Corrosion product | α - F_e | $F_e O$ | F_eO_4 | α, γ - $F_{e_2}O_3$ | α,γ,δ,β- F _e 00H | $F_e(OH)_2$ | $F_e(OH)_3$ | $F_{e_2}O_3\cdot 3H_2O$ |
|------------------------|------------------|---------|----------|---------------------------------|--------------------------------|-------------|-------------|-------------------------|
| Volume ratio, <i>c</i> | 1 | 1.5-1.8 | 2.0 | 2.0-2.1 | 2.8-3.5 | 3.8 | 3.0 | 6.0 |

Integrating Eqs. (9) and (10) into Eq. (11), the pit depth d can be estimated from the measurements of wavelength change of the FOSs:

For FBG sensors:

$$d = \frac{0.6L_0}{c - 1} \sqrt{\alpha \cdot \Delta \lambda_B (\alpha \cdot \Delta \lambda_B + 2)}$$
 (12)

$$d = \frac{0.6L_0}{c - 1} \sqrt{\beta \cdot \Delta \lambda_D (\beta \cdot \Delta \lambda_D + 2)}$$
(13)

244 2.3.2 Corrosion rate estimation

The corrosion loss-time model, a widely accepted approach that integrates a resilient probabilistic framework, stands as a testament to its adeptness in estimating corrosion rates. This model adeptly accounts for the innate uncertainty and variability innate to stochastic processes [53], offering a robust methodology for precise estimations. Its effectiveness, notably evidenced in various studies, especially in evaluating pitting corrosion on steel under prolonged immersion conditions, further underscores its reliability and applicability [54]. Hence, leveraging the validated prowess of this model, it was embraced as the linchpin for evaluating the corrosion rate in this investigation, ensuring a comprehensive and accurate assessment of corrosion dynamics.

The total mass loss m caused by corrosion can be calculated by:

$$m = \rho V \tag{14}$$

- where ρ is the density of corrosion product, and V is the volume of the corrosion product. Based
- on the assumption that the corrosion product mainly develops vertically, the volume of corrosion
- 256 product V is proportional to the corrosion-induced displacement Δ_c , as shown in Eq. (13):

$$V = k_1 \cdot \Delta_c \tag{15}$$

- where k_1 is the linear scaling factor between the volume of corrosion product and the corrosion
- induced upward displacement [40]. Combining Eqs. (13) and (14), the mass loss can be estimated
- 259 as:

245

246

247

248

249

250

251

252

253

$$m = \rho k_1 \cdot \Delta_c \tag{16}$$

- The corrosion rate (CR) is defined as the derivative of the total mass loss of a metal with respect to time. Integrating Eqs. (12) and (13), CR can be estimated as:
- For FBG sensors:

$$CR = \gamma \cdot \frac{d\sqrt{\alpha \cdot \Delta \lambda_B (\alpha \cdot \Delta \lambda_B + 2)}}{dt}$$
(17)

For OFDR-based DFOSs:

$$CR = \gamma \cdot \frac{d\sqrt{\beta \cdot \Delta \lambda_D (\beta \cdot \Delta \lambda_D + 2)}}{dt}$$
 (18)

where $\gamma = \frac{0.6\rho k_1 L_0}{c-1}$ is the sensitivity of the sensor to the corrosion rate of the metal, which can be calibrated with the known corrosion rate of a certain metal. Thus, the solution for corrosion rate can be obtained from the measured wavelength change of the FOSs.

3 Experimental program

264

265

266

267

268

269

270

271

272

273

274

275

276

277

278

279

280

281

282

283

284

285

286287

288

3.1 Materials and specimens

The ASTM A36 hot-rolled steel plate, measured with $170 \times 170 \times 3$ mm, were used in the experiment. To secure the plates on a test table, four holes with a diameter of 13mm were punched at the corners of each steel plate, as shown in Fig. 5 (a). Prior to installing the fiber optic sensors, steel plate surfaces were thoroughly cleaned with acetone to improve epoxy coating adhesion. Subsequently, both FBG sensors and DFOSs were placed on the steel plates, as shown in Fig. 5(b). Each plate was equipped with a 2-meter OFDR-based DFOS for corrosion distribution monitoring and an FBG sensor for dynamic response monitoring. The DFOS was configured in a serpentine pattern with 11 sensing segments, each measuring 100mm in length and spaced 10mm apart, covering a 100×100mm area. Each sensing segment and Bragg grating period were attached using super glue, with tape securing the U-turns. To distinguish the multiple distributed sensing segments for each specimen, they were labeled numerically from 1 to 11. The DFOS was connected to a LUNA ODiSI 6100 series distributed interrogator using a stand-off cable. The FBG sensor was mounted with super glue near the intermediate (No. 6) distributed sensing segment, where impact loads were expected. The FBG sensors were connected to an FBG high-frequency interrogator (LUNA si155 series) with a 500Hz acquisition frequency. Upon equipping the specimens with FOSs, a 1.5mm thick layer of DuralcoTM 4461 adhesive epoxy coating was applied to emulate industrial usage conditions and protect the optical fibers against damage from impact loads.

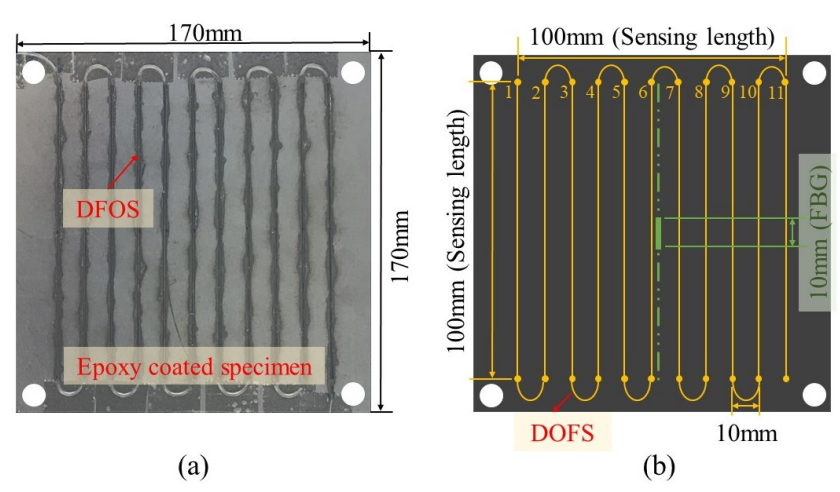


Fig. 5 (a) An example of the test specimens, and (b) schematic diagram of the sensor deployment.

3.2 Experimental set-up

289

290

291

292

293

294

295

296

297

298

299

300301

302

303

304

305

306

307308

309

310311

312

The interaction between corrosive agents and impact loads on epoxy-coated steel was explored through three sets of scenarios: impact loads only, corrosion only, and combined impact loads and corrosion. The impact loads were applied by a 2-kg calibration weight dropped freely at the center of the specimen, as shown in Fig. 6(a), with its position ensured by a rubber tube. Impact load tests involved a repetitive cycle conducted at various heights, h, (12.5mm, 25mm, and 50mm) with a 5-second contact time, repeated every 10 minutes. Assuming in the absence of air resistance, the impact velocity (v) and force (F_i) were determined at different impact heights employing Newton's laws of motion, where $v = \sqrt{2gh}$ and $F_i = \frac{mv^2}{2h}$. The calculated impact velocities and forces corresponding to each specific impact height are presented in Table 3. For the corrosion tests as shown in Fig. 6(b), since the distributed sensor was deployed in a 100mm × 100mm square, a PVC pipe with a diameter of 100 mm was fixed at the center of the test sample and filled with 3.5% NaCl solution to create an immersion corrosion environment, so the sensing area could cover the entire corrosive area. A 20mm artificial crack, created by a soft 25mm diameter grinding wheel, was placed 2mm from the FBG sensor to stimulate sensor-underlying corrosion. The corrosion tests lasted 43 days (1032 hours). The test set-up, illustrated in Fig. 6(c), allowed for the assessment of the combined effects of impact loading and corrosion. Importantly, in each impact cycle, the solution was extracted first, and then applied the dropping weight from various heights. Due to the short time intervals between the impact loadings, it is reasonable to assume that the corrosion conditions were not influenced during the loading apply. The impact cycle was repeated every six days during the corrosion process, continuing until sensor failure.







(a) Impact loading test

(b) Corrosion test

(c) Combined test

Fig. 6 Demonstration of the test set-ups.

Table 3 Impact load parameters.

| Impact height (mm) | Velocity (m/s) | Force (N) |
|--------------------|----------------|-----------|
| 12.5 | 0.5 | 30 |
| 25.0 | 0.7 | 35 |
| 50.0 | 1.0 | 40 |
| - | | |

3.3 Specimen numbering rules

A total of 12 epoxy-coated steel plates were tested, with 4 in each group, including one specimen for temperature compensation. Consequently, Eqs. (3) and (5) are applicable. Considering that the drop weight was released from three different heights with six impact cycles, each specimen underwent 18 working cases. Table 4 illustrates the specimen groups and the numbering rules for all test specimens. For example, C1 stands for specimen No. 1 subjected to corrosion conditions only; I3 stands for specimen No. 3 subjected to impact load conditions only, with the impactor released from heights of 12.5, 25.0, and 50.0 mm, respectively, in a complete impact cycle; M2 stands for specimen No. 2 subjected to the combined conditions of impact loads and corrosion, with the impactor released from heights of 12.5, 25.0, and 50.0 mm, respectively, in a complete impact cycle.

Table 4 Investigated cases under different conditions.

| Specimen | Notes |
|----------|---|
| C1 | Specimen No.1 subjected to corrosion conditions only |
| I3 | Specimen No.3 subjected to impact loads conditions only |
| M2 | Specimen No.2 subjected to combined impact loads and corrosion conditions |

4 Experimental results and discussions

4.1 Validation of fiber optic-based sensing model

Fig. 7 (a)-(c) depict the Bragg wavelength changes of the specimens of I1, I2, and I3 under impact loads from different heights, respectively. The strain induced by external loads of all the specimens recovered after approximately 5 seconds. It is evident that the wavelength changes return to zero following the unloading of the impact loads, signifying the presence of elastic strain resulting from the impactor's descent from heights of 12.5, 25.0, and 50.0 mm during the impact loading test. Given this observation, in the combined corrosion and impact loading conditions, the detected strain is attributed to corrosion products rather than the impact loads. Consequently, Eqs. (12) and (13) can be applied to calculate the pit depth. In addition, it can be seen that the FBG sensors are capable of capturing the transient load-induced strains due to their high-frequency response, allowing to record and monitor rapidly changing signals or events.

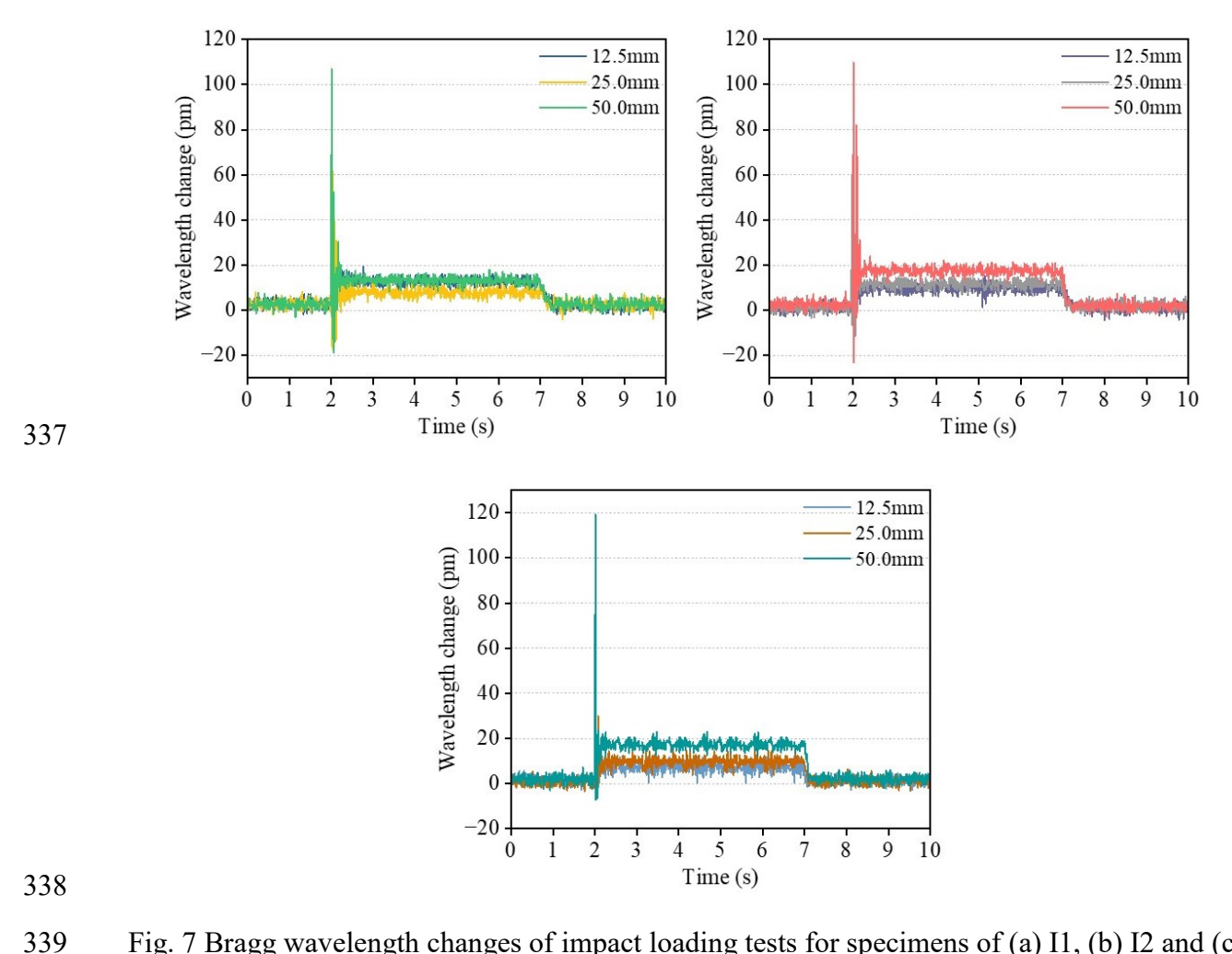


Fig. 7 Bragg wavelength changes of impact loading tests for specimens of (a) I1, (b) I2 and (c) I3.

The Keyence Digital Microscope was used to scan the pit depth of the test specimens subjected to corrosion only and combined impact loads and corrosion. Fig. 8 shows the comparison between estimated pit depths using Eq. (12) and the scanned depths. Clearly, the scanned depths closely align with the estimated values, showing a maximum discrepancy of 1.11%, and the minimum discrepancy was just 0.18%. Also, it is noteworthy that the scanned pit depths were marginally smaller than the calculated values, possibly due to residual corrosion products in the pits. This close alignment between estimated and scanned pit depths corroborates the accuracy of the proposed pit depth model based on FBG sensors. Thus, the FBG-based sensing model is applicable to corrosion monitoring under the corrosion only and combined impact loads and corrosion conditions.

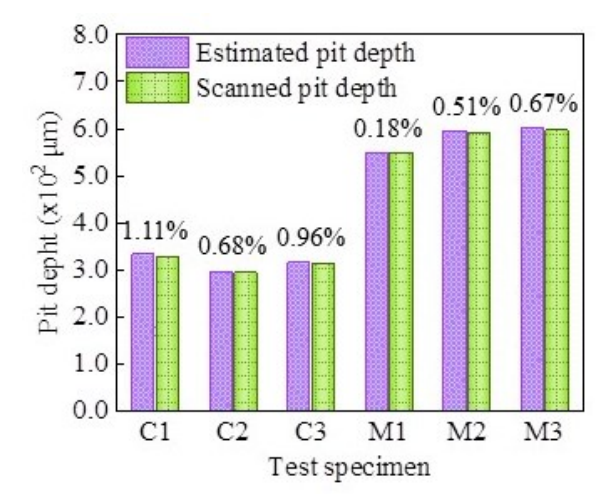


Fig. 8 Comparison between the FBG-based estimation of the pit depth and scanned pit depth.

The DOFS suffered damage during the 4th impact cycle. To make a better comparison of the strain changes throughout the complete corrosion durations, we used the data obtained from the corrosion-only test herein. Fig. 9 shows the strain changes monitored by the FBG sensors and DFOSs under corrosion-only conditions. The wavelength changes are measured at the adjacent points where FBG and DFOS were located. It can be seen that the strain changes closely match between the FBG and DOFSs for all the specimens from C1 to C3, indicating the applicability and accuracy of the DFOS-based sensing principle. Thus, the fiber optic-based sensing models in terms of both FBG and DOFS are valid for corrosion monitoring and assessment.

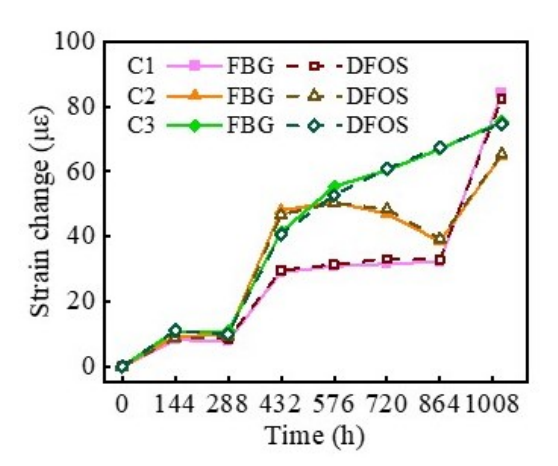


Fig. 9 Strain changes of FBG and DFOS under corrosion-only condition.

4.2 Effects of the impact loads on corrosion severity

4.2.1 Mass loss

The mass-loss assessment quantifies the extent of corrosion by measuring the difference in specimen mass before and after exposure to corrosive agents. This method serves as one of the fundamental means of quantitatively evaluating corrosion levels. It is particularly relevant in cases

where pitting corrosion is significantly severe while uniform corrosion remains relatively minimal [55]. Fig. 10 illustrates the visual comparisons of specimens subjected to corrosion only and those exposed to combined impact loads and corrosion conditions. It is evident that more severe corrosion damage was observed in specimens subjected to combined conditioning. This suggests that impact loads can exacerbate the degree of corrosion.

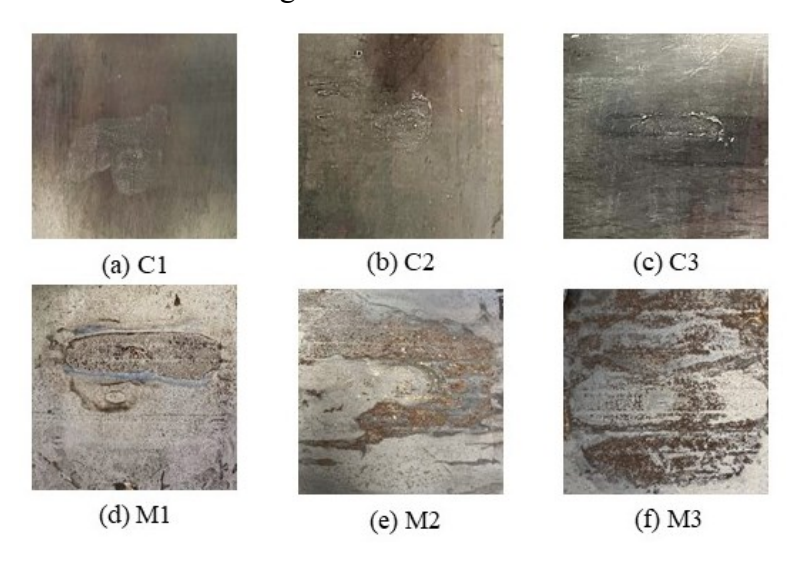


Fig. 10 Visual inspection of specimens after rust removal.

The mass loss assessment procedure consists of the following steps: initially, the initial mass of each sample is measured using a precision electronic scale (0.01g accuracy) before sensor installation and corrosion testing. Subsequently, the samples are subjected to environmental exposure and immersed in an acetone-filled digital ultrasonic cleaner to remove the sensors, epoxy coatings, and accumulated corrosion products from the sample surfaces. Afterward, the samples are placed in plastic containers with desiccants for 24 hours to ensure complete drying, and finally, the mass of the corroded sample is measured and compared to its initial mass. The mass loss ratio (η_m) of all the solution conditioned specimens was calculated using Eq. (19),

$$\eta_m = \frac{m_0 - m_t}{m_0} \times 100\% \tag{19}$$

where m_0 is the original mass; m_t is the residual mass of after rust removal. Table 5 provides details on the mass loss ratios of the specimens and their corresponding statistical characteristics, with μ representing the mean value and σ representing the standard deviation. Generally, the mass loss ratios of the specimens under corrosion conditions were notably larger than those subjected to combined conditioning. The mean mass loss ratios were 0.30% and 0.56%, respectively, indicating more severe damage occurred in the specimens exposed to combined conditioning. These results align with the visual inspections shown in Fig. 10. Furthermore, the magnification factor is defined as the mean value of the mass loss ratio under combined conditioning divided by that under corrosion conditioning, calculated to be 1.66. This indicates that the impact loads

exacerbate mass loss due to corrosion. This observation can be attributed to the impact loads disrupting the inhibitory effect of rusts on corrosion progression, thereby causing the formed pits to continue growing and merging into larger pits, which is consistent with the visual inspection in Fig. 10.

Table 5 Mass loss ratios and statistical characteristics.

| Specimen | Original mass (g) | Residual mass (g) | η_m (%) | μ (%) | σ (%) | Magnification factor |
|-----------|----------------------|--------------------|--------------|-------|-------|----------------------|
| Corrosion | conditioned | | | | | |
| C1 | 671.23 | 669.07 | 0.32 | 0.30 | 0.015 | \ |
| C2 | 672.09 | 670.17 | 0.29 | | | \ |
| C3 | 672.75 | 670.7 | 0.30 | | | \ |
| Combined | impact loads and cor | rosion conditioned | | | | |
| M1 | 673.56 | 669.99 | 0.53 | 0.56 | 0.026 | 1.66 |
| M2 | 673.88 | 670.01 | 0.57 | | | \ |
| M3 | 672.51 | 668.60 | 0.58 | | | \ |

4.2.2 Pit depth

Table 6 details the pit depths located in the center of the steel plate subjected to corrosion only and combined conditioning, with calculations based on Eq. (12), where the exposure time t is expressed in hours. The mean pit depth (d_{mean}) was calculated using the FBG sensing model, and σ is the standard deviation, which are all expressed in μm . It is worth noting that the impactor was dropped from different heights with a time interval of 10 minutes, and it is assumed that such a short time interval will not have any influence on corrosion development. This assumption is supported by observations that the Bragg wavelength of C1, C2, and C3 did not change within 10 minutes during each impact cycle. when the 6th impact cycle was completed, the FBG sensors continued recording until then end of t = 1032.33 hours in order to monitor the response after the impact loads.

Table 6 Pit depth estimated based on the FBG sensors $(10^2 \mu m)$.

| Impact cycle | t(h) | h (mm) | C1 | C2 | C3 | d_{mean} | σ | M1 | M2 | M3 | d_{mean} | σ |
|-----------------|--------|--------|------|------|------|------------|------|------|------|------|------------|------|
| 1 st | 144 | 12.5 | 0.91 | 0.75 | 0.67 | 0.78 | 0.10 | 1.86 | 1.10 | 1.29 | 1.42 | 0.32 |
| | 144.16 | 25.0 | | | | | | 1.80 | 1.25 | 1.87 | 1.64 | 0.28 |
| | 144.33 | 50.0 | | | | | | 1.74 | 2.05 | 2.23 | 2.01 | 0.20 |

| 2 nd | 288 | 12.5 | 2.07 | 1.73 | 1.65 | 1.82 | 0.18 | 2.81 | 3.31 | 3.46 | 3.19 | 0.28 |
|-----------------|---------|------|------|------|------|------|------|------|------|------|------|------|
| | 288.16 | 25.0 | | | | | | 2.83 | 3.85 | 3.95 | 3.54 | 0.51 |
| | 288.33 | 50.0 | | | | | | 3.74 | 4.63 | 4.87 | 4.41 | 0.49 |
| $3^{\rm rd}$ | 432 | 12.5 | 1.95 | 2.62 | 2.37 | 2.32 | 0.28 | 4.05 | 5.00 | 5.12 | 4.72 | 0.48 |
| | 432.16 | 25.0 | | | | | | 4.18 | 5.02 | 5.18 | 4.79 | 0.44 |
| | 432.33 | 50.0 | | | | | | 5.20 | 6.16 | 6.36 | 5.91 | 0.50 |
| 4 th | 576 | 12.5 | 2.04 | 2.64 | 2.83 | 2.50 | 0.34 | 4.33 | 5.30 | 5.61 | 5.08 | 0.55 |
| | 576.16 | 25.0 | | | | | | 4.44 | 5.43 | 5.71 | 5.19 | 0.55 |
| | 576.33 | 50.0 | | | | | | 5.84 | 6.76 | 7.05 | 6.55 | 0.52 |
| 5 th | 720 | 12.5 | 2.10 | 2.67 | 2.90 | 2.56 | 0.34 | 4.64 | 5.64 | 5.90 | 5.39 | 0.54 |
| | 720.16 | 25.0 | | | | | | 4.86 | 5.78 | 6.00 | 5.54 | 0.49 |
| | 720.33 | 50.0 | | | | | | 6.43 | 7.31 | 7.48 | 7.07 | 0.46 |
| 6^{th} | 864 | 12.5 | 2.13 | 2.72 | 2.94 | 2.60 | 0.34 | 5.02 | 5.82 | 5.99 | 5.61 | 0.42 |
| | 864.16 | 25.0 | | | | | | 5.31 | 6.04 | 6.18 | 5.84 | 0.38 |
| | 864.33 | 50.0 | | | | | | 6.94 | 7.67 | 7.77 | 7.46 | 0.37 |
| \ | 1032 | \ | 2.81 | 2.44 | 2.63 | 2.62 | 0.15 | 5.48 | 5.93 | 6.00 | 5.80 | 0.23 |
| \ | 1032.16 | \ | | | | | | 5.54 | 6.28 | 6.41 | 6.08 | 0.38 |
| End | 1032.33 | \ | | | | | | 7.23 | 7.96 | 8.06 | 7.75 | 0.37 |

Clearly, two general trends can be observed from Table 6. First, the pit depths of all the specimens increased over time, indicating pit depth development in a chloride-rich environment and under the influence of corrosive agents coupled with external impact loads. This phenomenon can be explained by the penetration mechanisms for pit initiation, which involve aggressive anions being transported through the passive film to reach the oxide interface, thereby promoting aggressive dissolution [56]. Meanwhile, the mechanism could be aided by the induction time for pitting and the presence of chloride in the electrolyte [57]. In the present study, the high chloride concentration, as well as the damaged epoxy coatings, caused and further accelerated the breakdown of the protective layer. Secondly, the specimens that underwent combined conditioning exhibited larger pit depths than those subjected to corrosion conditioning alone. Specifically, the mean pit depths of M1, M2, and M3 in each complete impact cycle were significantly greater than the mean pit depths of C1, C2, and C3. This can be attributed to film rupture occurring as a result of mechanical stress at vulnerable locations or imperfections, leading to localized breakdown

 events [58]. To statistically assess the effect of the impact loads on pit depth development, the Mann-Whitney U test was conducted. The *p*-value for the mean pit depths between corrosion-only and combined conditioning was found to be less than 0.05, indicating significant differences in pit depth development with and without the presence of impact loads.

4.2.3 Incipient corrosion development

426

427

428

429

430

431

432

433

434

435

436

437

438 439

440

441

442

443

444

445

446

447

448

449

450

451

452

453

454

455

456

457

458

459

It is generally recognized that the long-term corrosion of steels, cast irons, and low-carbon alloys exhibits a distinctive bi-modal trend characterized by the presence of two dominant corrosion modes that manifest over extended periods of exposure to corrosive environments, such as atmospheric exposures, fresh water immersion, and marine immersion [59, 60]. The first mode occurs under oxygenated conditions, where corrosion is typically slower and exhibits different characteristics compared to the second mode, which occurs under anoxic conditions where corrosion rates tend to accelerate. This dual-phase behavior highlights the intricate interplay between environmental factors and material properties. The transition point that distinguishes between the two modes can vary from 1 to 5 years depending on the stochastic corrosion processes that steels undergo in various settings [54]. This study focuses on investigating the incipient corrosion mode from pit initiation to propagation under the impact loading stimulations.

Fig. 11 shows the Bragg wavelength changes due to individual corrosion and combined conditioning. In Fig. 11 (a), the wavelength shifts of C1, C2 and C3 exhibits distinct three phase pattern, which is consistent with the observations in [53, 61, 62]. Phase 0, characterized by the initial onset of corrosion, was governed by the kinetic phase for a very short time period, during which rust formed and filled gaps between the adhesive and sensors; Phase 1, rapid corrosion development due to the oxygen concentration in the electrolyte surrounding the metal surface; and Phase 2, slower corrosion progression due to the obstruction of oxygen diffusion by accumulated corrosion products. The remaining wavelength changes primarily reflected residual strain. Throughout the total 1032 hours of corrosion exposure, phase 0, 1, and 2 lasted approximately 290 hours, 175 hours, and 567 hours, respectively. In comparison, Fig. 11 (b) shows the combined Bragg waveforms. While corrosion phases showed gradual wavelength changes, impact responses resulted in sudden increases. It can be observed that the difference in wavelength changes induced by corrosion and impact loads were up to 100 pm. Since the load-induced strain can be recovered to zero after approximately 5 seconds as discussed in Fig. 7, this suggests that impact loads intensified corrosion. Upon comparing total Bragg wavelength shifts between individual corrosion and combined scenarios, it is apparent that impacts substantially promoted corrosion growth, which is consistent with the statistical characteristics with regard to the p-values. For instance, specimens C3 and M3 recorded total wavelength changes of 90.93 and 627.45 pm, respectively, which represents a 6.9-fold increase due to impact loading. Furthermore, it is noted that the impact exerted varying degrees of acceleration on corrosion. In Fig. 11 (a), similar overall wavelength changes were observed in C1, C2, and C3. However, end-test wavelength changes for M1, M2, and M3 significantly differed, at 362.92, 522.95, and 627.45 pm, respectively, as shown in Fig. 11

(b). This can be attributed to disparities in coating porosity or the bonding characteristics between the coating and steel, leading to varying influences on corrosion.

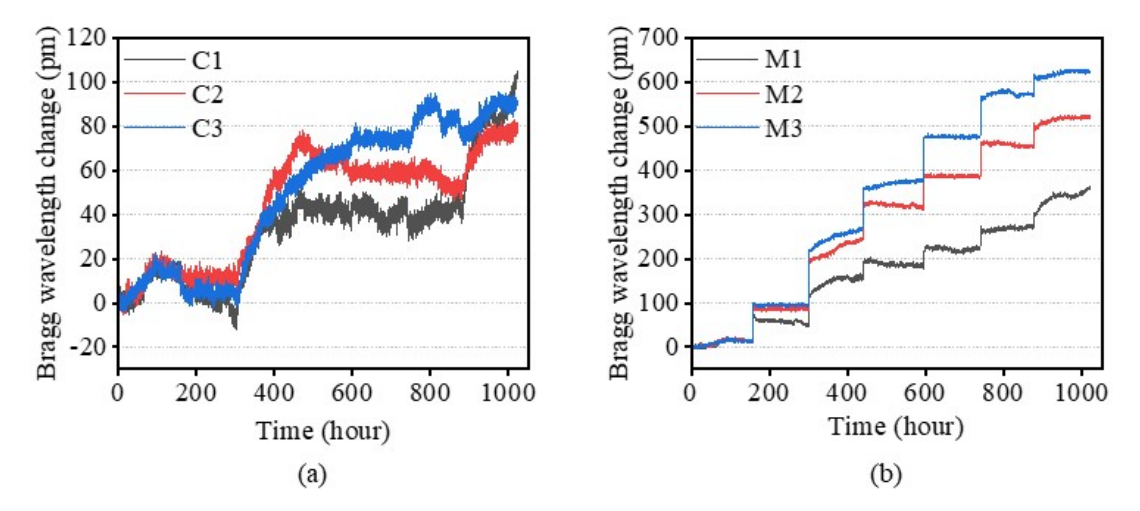
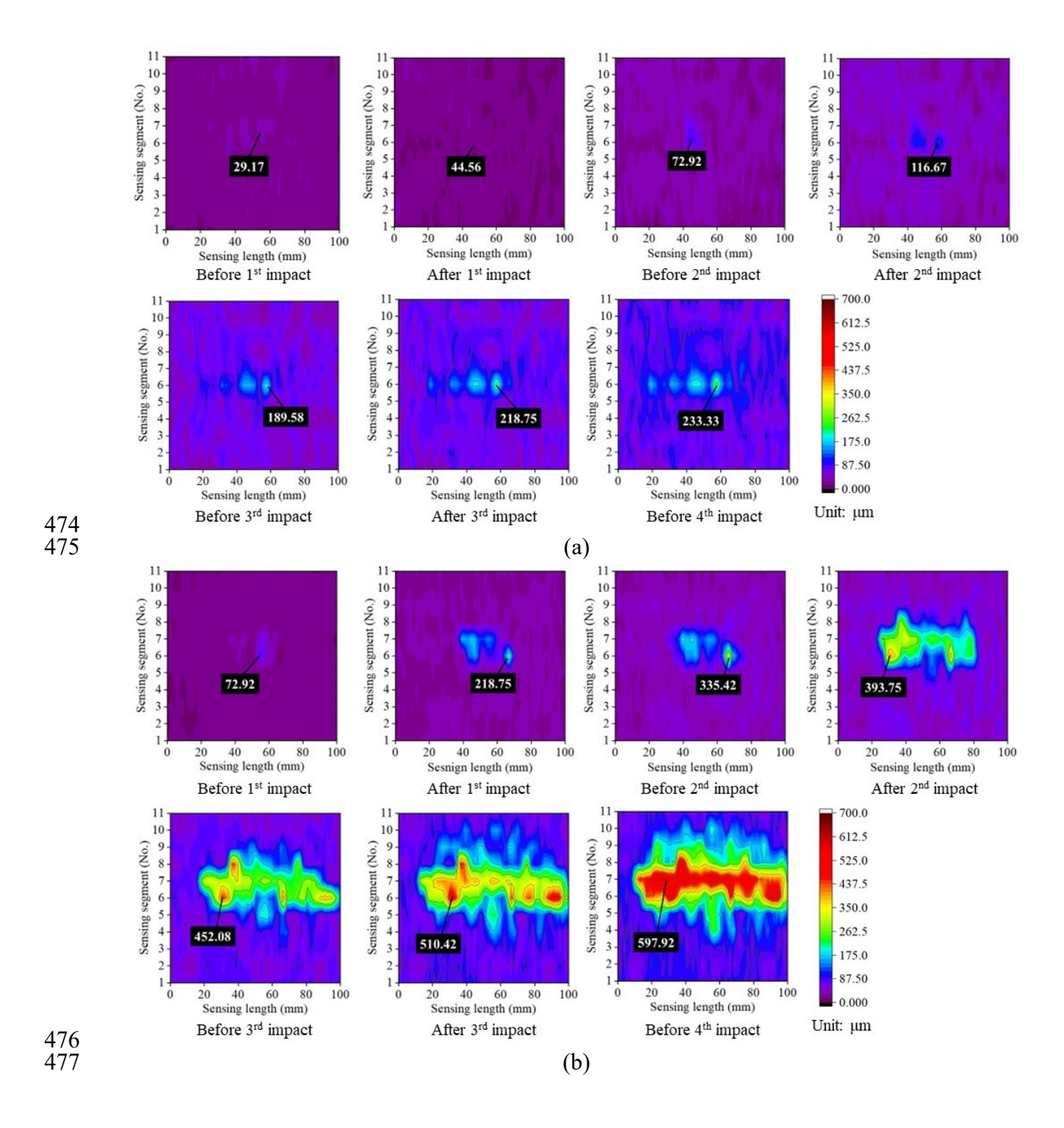


Fig. 11 Bragg wavelength change: (a) corrosion only test, and (b) combined corrosion and impact test.

To counter the constraints of FBG sensors, DFOSs were applied for real-time monitoring of corrosion growth and spread. Fig. 12 (a)-(c) illustrate the incipient corrosion distribution before and after each impact cycle for specimens M1, M2, and M3, revealing the expansion of corrosion damage after impact loading. Corrosion initiated in areas where cracks appeared in the epoxy coating and then intensified and spread over time. However, the brittleness of distributed fibers caused premature damage to DFOSs before the 4th impact cycle test. Although corrosion process monitoring was incomplete, the DFOS-detected corrosion profiles could predict those were observed in visual inspections with similar corresponding patterns, as shown in Fig. 10, confirming their efficacy in tracing corrosion progression and validating visual inspection findings.



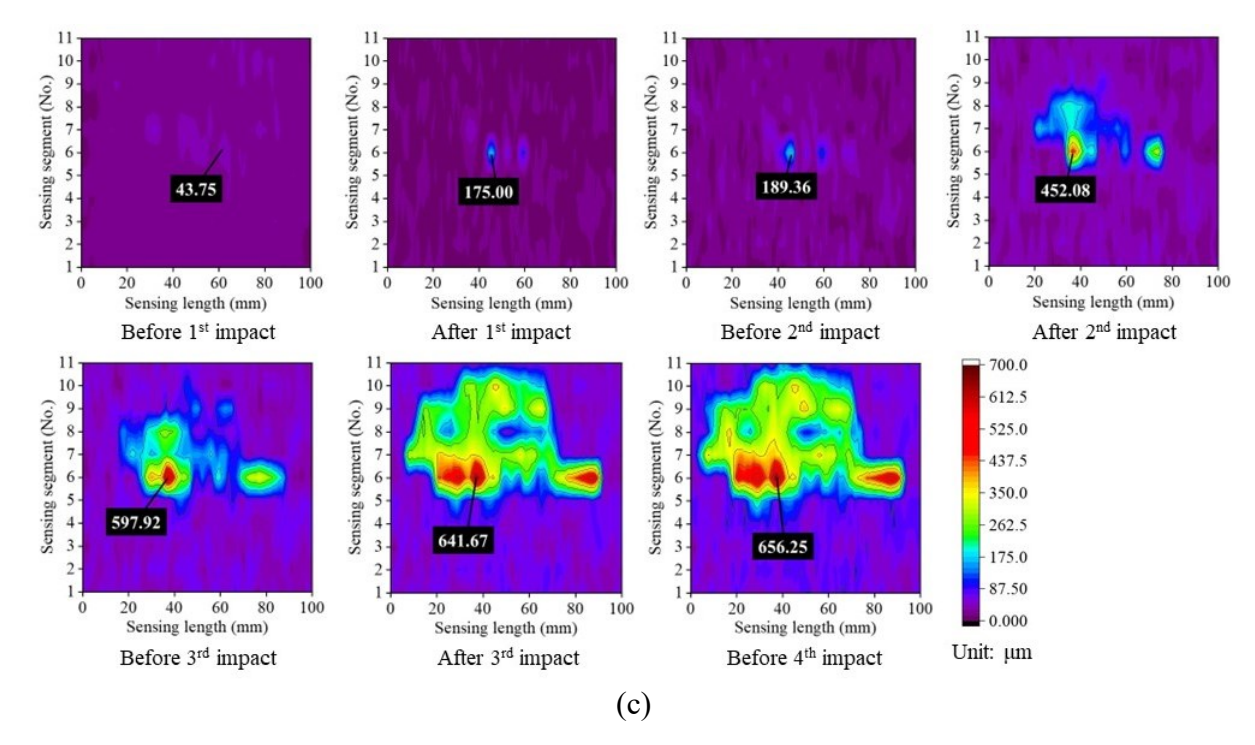


Fig. 12 The effect of impact on corrosion distribution for specimens (a) M1 (b) M2 and (c) M3.

4.3 Time-dependent corrosion wastage model

4.3.1 Effect of impact loads on pit evolution

Pitting corrosion is notably hazardous due to its localized and often unpredictable nature. The initiation of pits is widely acknowledged to occur in durations as short as microseconds [63], influenced by various factors such as improper maintenance procedures, coating damage, and environmental conditions [64]. As illustrated in Fig. 1, unlike uniform corrosion, which gradually erodes a material's surface uniformly, pitting corrosion creates small, concentrated cavities or pits that can rapidly penetrate deep into the material. These pits serve as initiation points for more severe structural damage, potentially leading to catastrophic failures. Moreover, pitting corrosion can occur without significant external signs, making it challenging to detect and mitigate in its early stages. Consequently, modeling incipient corrosion is of paramount importance in ensuring the safety and longevity of various industrial and infrastructure assets.

To demonstrate the time-dependent stochastic process of pitting corrosion, the mean pit depth (d_{mean}) could be fitted using the widely adopted power-law function $d(t) = A \cdot t^B$ or the semilog function $d(t) = A + B \cdot log(t)$, where A and B are fitting parameters. However, this was found not to be a well-fitted function [54]. In this study, the Weibull function was used to model the incipient corrosion loss in terms of pit depth, as illustrated in Eq. (20) [65, 66]:

$$d(t) = d_{lim} \cdot [1 - exp(-(A \cdot t)^B)]$$
(20)

where d_{lim} is the upper limit of pit depth; A and B are the shape and scale parameters of pit depth, respectively.

Fig. 13 (a)-(c) show the Weibull function-based modeling of the pit depth evolution under different conditions. It can be seen that the Weibull function fits well the data of the mean pit depth, with the smallest coefficient of determination R^2 of 0.998. The mean pit depths of the specimens subjected to combined conditioning were apparently larger than those of the specimens subjected to corrosion only conditioning. For example, in Fig. 13 (a), the mean pit depth of the specimens without impact loads increased up to approximately $230\mu m$, compared with the mean pit depth with 12.5mm impact loads increased to approximately $600\mu m$. Similar evolution patterns of the mean pit depth can also be found in Fig. 13 (b) and (c) for different dropping heights. This observation can be attributed to the fact that the impact loads disrupted inhibitory effect of the formed corrosion products and thus facilitated the diffusion-controlled oxygen reduction. Meanwhile, combined with the delamination of the coating allowing for further passive film breakdown in the presence of aggressive anionic species, and the pitting severity tends to deteriorate with the chloride concentrations [58].

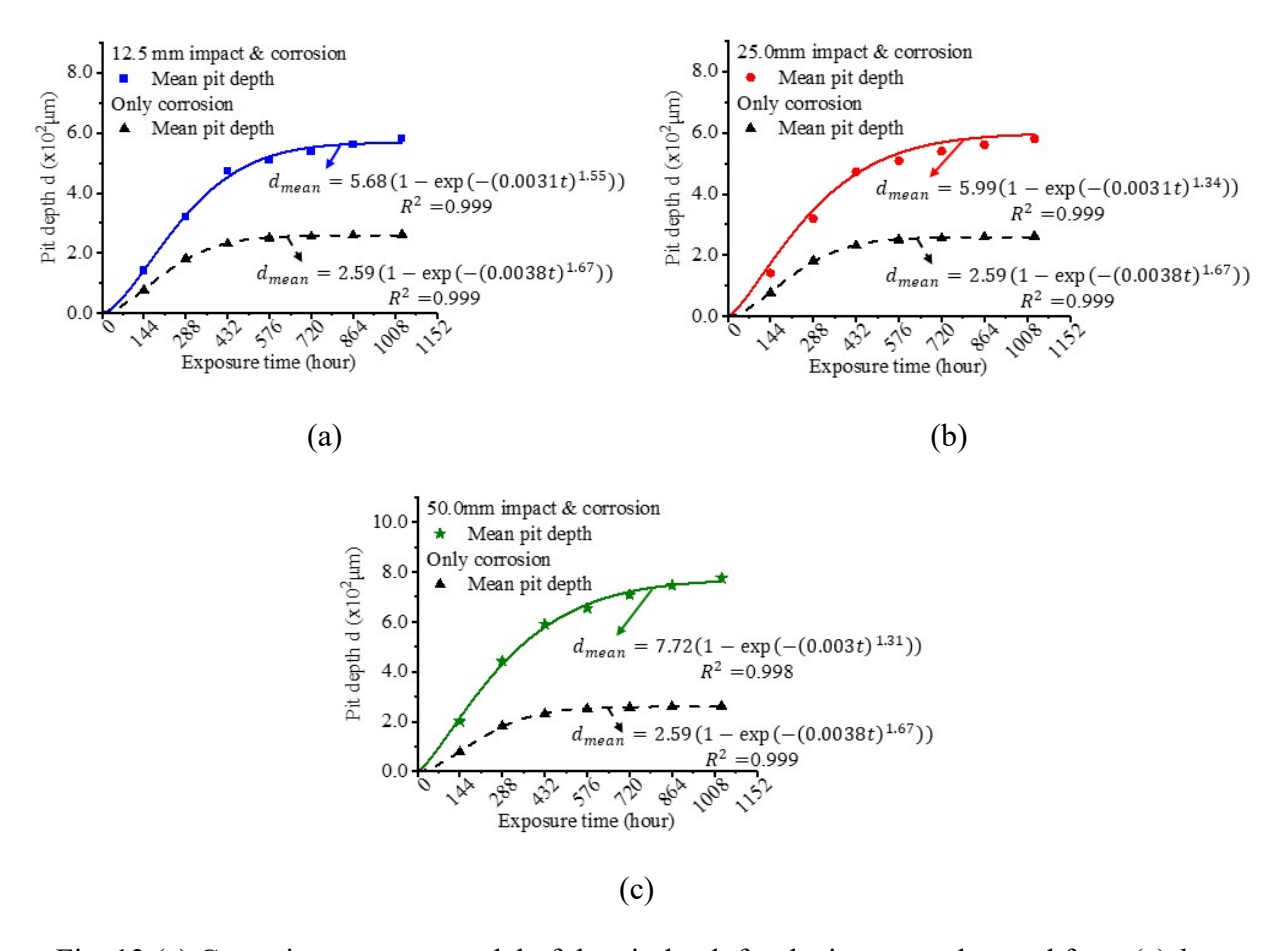


Fig. 13 (a) Corrosion wastage model of the pit depth for the impactor dropped from (a) h = 12.5mm, (b) h = 25.0mm, and (c) h = 50.0mm.

4.3.2 Effect of impact loads on corrosion rate

515

516

517

518

519

520

521

522

523

524

525

526

527

528529

530

531532

533

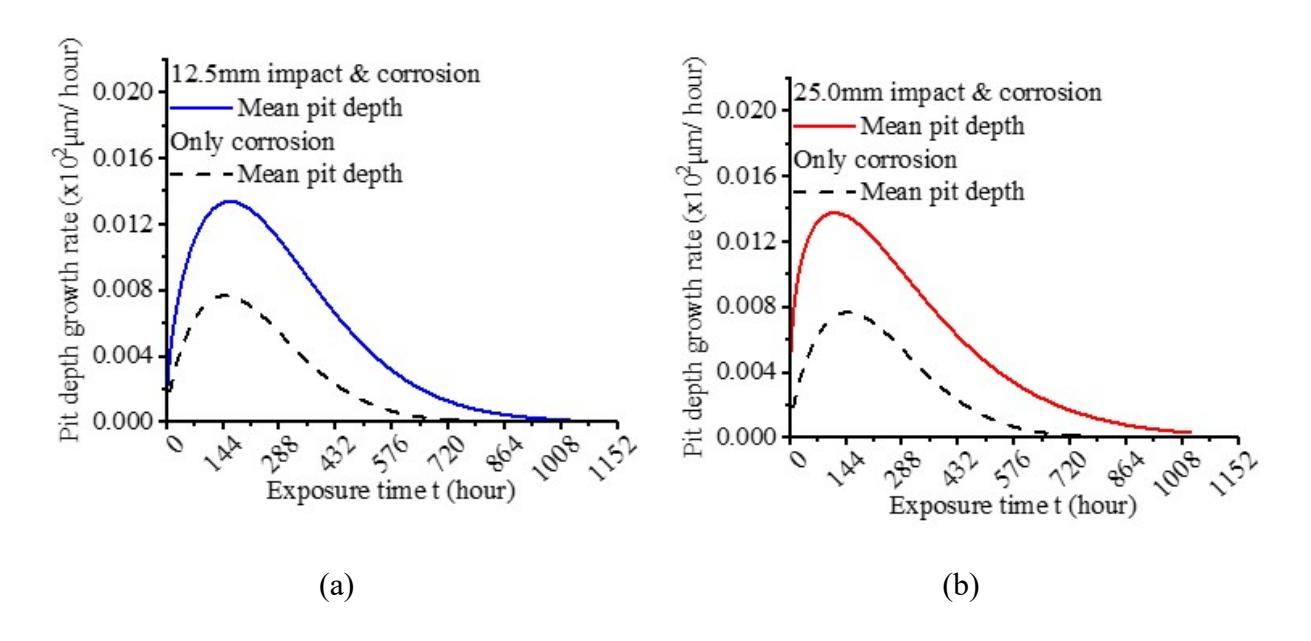
534

535

The corrosion rate can be calculated using the derivative of the pit depth in terms of time, as shown in Eq. (21):

$$CR = \frac{\partial d(t)}{\partial t} = d_{lim} \cdot BA^B t^{B-1} \exp(-(A \cdot t)^B)$$
 (21)

Fig. 14 (a)-(c) show the corrosion rate (CR) of the mean pit depth for the impactor dropped from different heights. It can be seen that the CR of all specimens experienced combined conditioning was apparently larger than that of the corrosion conditioned specimens. This indicates the impact loads accelerate the pit evolution over time. The highest CR typically manifested in a couple of days following the onset of corrosion, which is consistent with the observations in [65]. This phenomenon can be attributed to several interrelated factors. Firstly, the mechanical action of impact loads can physically damage the protective oxide layer on the metal's surface, exposing fresh metal to the corrosive environment and accelerating the corrosion process. Additionally, the combination of mechanical stress from impact loads and the corrosive environment can lead to stress-corrosion cracking, wherein the stress creates micro-cracks on the metal surface that serve as initiation points for corrosion [67, 68]. Impact loads can also disrupt the stagnant layer of solution near the metal surface, facilitating better mass transport of corrosive ions and thereby increasing the corrosion rate [3]. Furthermore, the electrochemical conditions at the metal's surface can be altered by the mechanical deformation caused by impact loads, potentially promoting a higher rate of electrochemical reactions associated with corrosion. The CR of the mean pit depth decreased monotonically with the exposure time, this can be attributed to the accumulation of rust products likely contributed to a decrease in oxygen diffusion, which in turn could have decelerated the corrosion process.



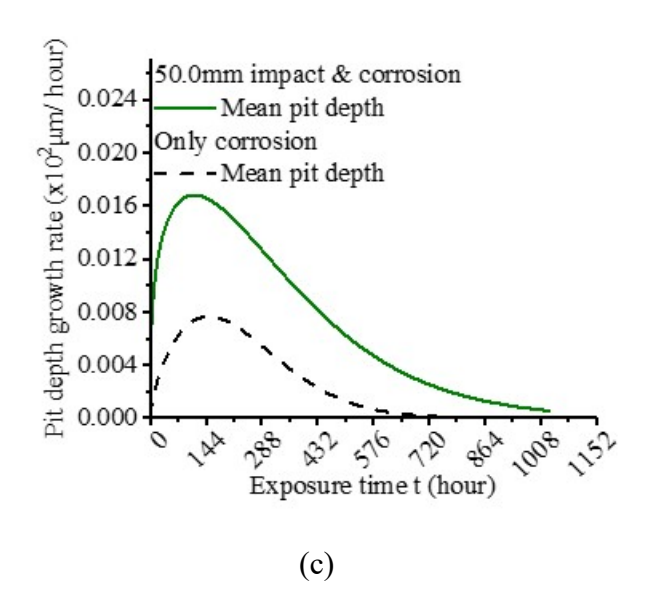
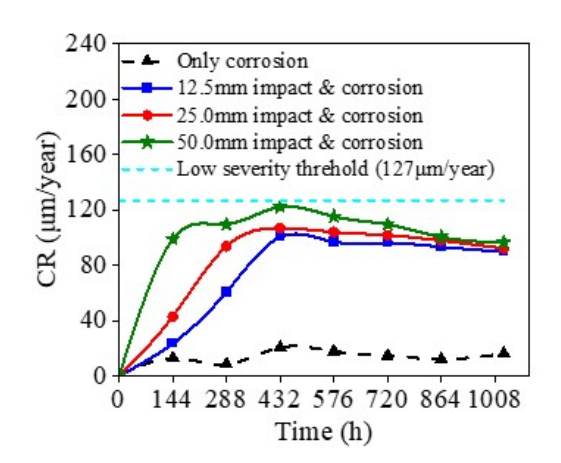


Fig. 14 (a) Corrosion rate for the impactor dropped from (a) h = 12.5mm, (b) h = 25.0mm, and (c) h = 50.0mm.

4.3.3 NACE severity ranking considering impact loads

The CR calculated using Eq. (21) varied throughout the corrosion process, as depicted in Fig. 15. It is evident that the CR for specimens subjected to combined conditions was significantly higher than for those under individual corrosion, indicating that impact loading accelerated the CR. Notably, there was a rapid increase in CR during the initial 432 hours of exposure due to impact load, which was prominent and gradually declined thereafter. Furthermore, the effect of impact load on CR varied substantially among specimens, with those experiencing severe coating damage showing a more pronounced impact. Referring to NACE specifications for pitting corrosion severity [69], corrosion rates are categorized into four levels: low, moderate, high, and severe, with corrosion rates below 127 μ m/year, 127-201 μ m/year, 203-381 μ m/year, and above 381 μ m/year, respectively. In Fig. 15, the CR of specimens all was below 127 μ m/year, suggesting low corrosion severity.



551

552

553

554

555556

557

558

559

560

561

562563

564

565

566

567

568

569

570

571

572

573

574

575

576

577578

579

580

581

582

583

584

588

5. Conclusions and future work

This paper presents an experimental investigation into the intricate interplay between impact loads and corrosion on steel plates, employing discrete and distributed FOSs to monitor structural responses and corrosion severity. The systematic strategy developed in this study yields several crucial conclusions. The generalized fiber optic-based sensing models were developed for both FBG and OFDR-based distributed sensors to calculate pit depth and corrosion rate. The accuracy of the sensing model for corrosion monitoring and assessment was demonstrated by the Keyence Digital Microscope. FBG sensors exhibited the highlighted high-frequency response and ability to capture transient impact loads at the specified site. In contrast, OFDR-based distributed sensors provided sensitivity to incipient corrosion development on larger spatial scales. The mass loss of the specimens subjected to only corrosion and combined conditioning was calculated, and the magnification factor was up to 1.66, clearly demonstrating the amplifying effect of impact loads on corrosion-induced mass loss. The mean pit depths were calculated using the FBG sensing model. Statistical analysis using the Mann-Whitney U test revealed a significant difference in pit depth development between conditions with and without the presence of impact loads. This clarifies the deeper pit depths observed in specimens exposed to combined conditions compared to those subjected to corrosion alone. The FBG sensors of the corrosion-conditioned specimens exhibited a distinct three-phase Bragg waveform, which reveals the mechanisms of the initiation and incipient progression of pitting corrosion. Meanwhile, the OFDR-based distributed sensors clearly show the distribution and prompt responses before and after the impact loads, demonstrating their capability for sensitivity on a larger spatial scale. Finally, a time-dependent corrosion wastage model was used to investigate the influence of the impact loads on corrosion severity. The mean pit depths of the specimens subjected to combined conditioning were apparently larger than those of the specimens subjected to corrosion only conditioning throughout the incipient pit evolutions. For engineering applications, the corrosion severity that considers the impact loads was calculated according to the NACE specification.

As this study was conducted in simulated corrosion environments, it is essential to validate the developed sensing platform through field testing scenarios. Furthermore, future research should focus on investigating the multiple interactions between mechanical structural damage and harsh environments. This will help broaden the understanding of the complex dynamics between mechanical factors and environmental conditions, leading to more comprehensive and accurate assessments of structural integrity in practical applications.

Acknowledgement

This work was supported by the United States National Science Foundation (NSF) [grant numbers CMMI-1750316 and OIA-2119691]; and United States Department of Transportation [grant number 693JK31950008CAAP].

References

589 [1] Koch GH, Brongers MP, Thompson NG, Virmani YP, Payer JH. Corrosion cost and preventive 590 strategies in the United States. United States. Federal Highway Administration; 2002.

- 591 [2] Jacobson GAJTB. NACE international's IMPACT study breaks new ground in corrosion
- management research and practice. 2016;46(2).
- 593 [3] Wasim M, Djukic MBJJoNGS, Engineering. External corrosion of oil and gas pipelines: A
- review of failure mechanisms and predictive preventions. 2022;100:104467.
- 595 [4] Kim C, Chen L, Wang H, Castaneda HJJoPS, Engineering. Global and local parameters for
- 596 characterizing and modeling external corrosion in underground coated steel pipelines: A review of
- 597 critical factors. 2021;1(1):17-35.
- 598 [5] Ginzel R, Kanters WJNn. Pipeline corrosion and cracking and the associated calibration
- considerations for same side sizing applications. 2002;7(07):1435-4934.
- 600 [6] Dastgerdi AA, Brenna A, Ormellese M, Pedeferri M, Bolzoni FJM, Corrosion. Electrochemical
- 601 methods for the determination of Pedeferri's diagram of stainless steel in chloride containing
- 602 environment. 2019;70(1):9-18.
- [7] Bazinet L, Ippersiel D, Gendron C, MAHDAVI B, AMIOT J, LAMARCHE FJJodr. Effect of
- added salt and increase in ionic strength on skim milk electroacidification performances.
- 605 2001;68(2):237-50.
- [8] Popoola LT, Grema AS, Latinwo GK, Gutti B, Balogun ASJIJoIC. Corrosion problems during
- oil and gas production and its mitigation. 2013;4:1-15.
- 608 [9] Gao K, Li D, Pang X, Yang SJCs. Corrosion behaviour of low-carbon bainitic steel under a
- 609 constant elastic load. 2010;52(10):3428-34.
- 610 [10] Zhang S, Pang X, Wang Y, Gao KJCs. Corrosion behavior of steel with different
- microstructures under various elastic loading conditions. 2013;75:293-9.
- 612 [11] Melchers RE, Paik JKJCs. Effect of tensile strain on the rate of marine corrosion of steel
- 613 plates. 2009;51(10):2298-303.
- [12] Dai M, Yang O, Xiao Y, Li FJM, Structures. Influence of longitudinal bar corrosion on impact
- 615 behavior of RC beams. 2016;49(9):3579-89.
- 616 [13] Dong W, Fang C, Yang SJBS. Influence of lateral impact on reinforced concrete piers under
- drying-wetting cycle and chloride ion corrosion environment. 2021;17(1-2):51-64.
- 618 [14] Qu H, Zhang W, Kou C, Feng R, Pan JJT-WS. Experimental investigation of corroded CHS
- tubes in the artificial marine environment subjected to impact loading. 2021;169:108485.
- 620 [15] Kumar S, Wang Y, Li M, Wang Q, Malathi S, Marques C, et al. Plasmon-based tapered-in-
- tapered fiber structure for p-cresol detection: From human healthcare to aquaculture application.
- 622 2022;22(19):18493-500.
- 623 [16] Liu X, Singh R, Li M, Li G, Min R, Marques C, et al. Plasmonic sensor based on offset-
- 624 splicing and waist-expanded taper using multicore fiber for detection of Aflatoxins B1 in critical

- 625 sectors. 2023;31(3):4783-802.
- 626 [17] Li G, Xu Q, Singh R, Zhang W, Marques C, Xie Y, et al. Graphene oxide/multiwalled carbon
- nanotubes assisted serial quadruple tapered structure-based LSPR sensor for glucose detection.
- 628 2022;22(17):16904-11.
- 629 [18] Soares MS, Silva LC, Vidal M, Loyez M, Facão M, Caucheteur C, et al. Label-free plasmonic
- immunosensor for cortisol detection in a D-shaped optical fiber. 2022;13(6):3259-74.
- [19] Wang Z, Wang G, Kumar S, Marques C, Min R, Li XJISJ. Recent advancements in resonant
- fiber optic gyro-a review. 2022.
- [20] Xu K, Chen Y, Okhai TA, Snyman LWJOME. Micro optical sensors based on avalanching
- silicon light-emitting devices monolithically integrated on chips. 2019;9(10):3985-97.
- 635 [21] Min R, Korganbayev S, Molardi C, Broadway C, Hu X, Caucheteur C, et al. Largely tunable
- dispersion chirped polymer FBG. 2018;43(20):5106-9.
- 637 [22] Leal-Junior A, Theodosiou A, Díaz C, Marques C, Pontes MJ, Kalli K, et al. Fiber Bragg
- 638 gratings in CYTOP fibers embedded in a 3D-printed flexible support for assessment of human-
- 639 robot interaction forces. 2018;11(11):2305.
- [23] Leal-Junior AG, Frizera A, Marques C, Pontes MJJISJ. Optical fiber specklegram sensors for
- mechanical measurements: A review. 2019;20(2):569-76.
- [24] Yan M, Wang J, Han E, Ke WJCS. Local environment under simulated disbonded coating on
- steel pipelines in soil solution. 2008;50(5):1331-9.
- 644 [25] Xu L, Shi S, Wang X, Yan F, Huang Y, editors. Investigating combined effects between
- dynamic mechanical loads and corrosion on epoxy coated steel using distributed fiber optic sensors.
- Optical Waveguide and Laser Sensors II; 2023: SPIE.
- [26] Bao Y, Huang Y, Hoehler MS, Chen GJS. Review of fiber optic sensors for structural fire
- 648 engineering. 2019;19(4):877.
- 649 [27] Gao J, Wu J, Li J, Zhao XJN, International E. Monitoring of corrosion in reinforced concrete
- structure using Bragg grating sensing. 2011;44(2):202-5.
- [28] Hu W, Cai H, Yang M, Tong X, Zhou C, Chen WJCS. Fe–C-coated fibre Bragg grating sensor
- 652 for steel corrosion monitoring. 2011;53(5):1933-8.
- 653 [29] Hassan MRA, Bakar MHA, Dambul K, Adikan FRMJS. Optical-based sensors for monitoring
- 654 corrosion of reinforcement rebar via an etched cladding Bragg grating. 2012;12(11):15820-6.
- 655 [30] Zheng Z, Sun X, Lei YJFoMEiC. Monitoring corrosion of reinforcement in concrete
- structures via fiber Bragg grating sensors. 2009;4:316-9.
- 657 [31] Xu L, Zhang D, Huang Y, Shi S, Pan H, Bao YJS. Monitoring Epoxy Coated Steel under
- 658 Combined Mechanical Loads and Corrosion Using Fiber Bragg Grating Sensors.

- 659 2022;22(20):8034.
- 660 [32] Sousa I, Pereira L, Mesquita E, Souza VL, Araújo WS, Cabral A, et al. Sensing system based
- on FBG for corrosion monitoring in metallic structures. 2022;22(16):5947.
- [33] Huang H, Jia C, Guo L, editors. Effect of local corrosion on tensile behavior of steel plates.
- Structures; 2022: Elsevier.
- 664 [34] Al Handawi K, Vahdati N, Rostron P, Lawand L, Shiryayev OJS, Chemical AB. Strain based
- FBG sensor for real-time corrosion rate monitoring in pre-stressed structures. 2016;236:276-85.
- 666 [35] Rodrigues C, Cavadas F, Félix C, Figueiras JJES. FBG based strain monitoring in the
- rehabilitation of a centenary metallic bridge. 2012;44:281-90.
- [36] Lei Y, Zheng Z-PJMPiE. Review of physical based monitoring techniques for condition
- assessment of corrosion in reinforced concrete. 2013;2013.
- 670 [37] Sun Y, Shi B, Chen S-e, Zhu H, Zhang D, Lu YJSSS. Feasibility study on corrosion
- monitoring of a concrete column with central rebar using BOTDR. 2014;13(1):41-53.
- [38] Mao J, Chen J, Cui L, Jin W, Xu C, He YJS. Monitoring the corrosion process of reinforced
- concrete using BOTDA and FBG sensors. 2015;15(4):8866-83.
- [39] Tan X, Fan L, Huang Y, Bao YJAiC. Detection, visualization, quantification, and warning of
- pipe corrosion using distributed fiber optic sensors. 2021;132:103953.
- 676 [40] Xu L, Shi S, Yan F, Huang Y, Bao YJSHM. Experimental study on combined effect of
- 677 mechanical loads and corrosion using tube-packaged long-gauge fiber Bragg grating sensors.
- 678 2023:14759217231164961.
- [41] Tan C, Shee Y, Yap B, Adikan FMJS, Physical AA. Fiber Bragg grating based sensing system:
- Early corrosion detection for structural health monitoring. 2016;246:123-8.
- [42] Xu KJJoM, Microengineering. Silicon electro-optic micro-modulator fabricated in standard
- 682 CMOS technology as components for all silicon monolithic integrated optoelectronic systems.
- 683 2021;31(5):054001.
- 684 [43] Wang H-P, Dai J-G, Wang X-Z. Improved temperature compensation of fiber Bragg grating-
- based sensors applied to structures under different loading conditions. Optical Fiber Technology.
- 686 2021;63:102506.
- [44] Bao X, Wang Y. Recent advancements in Rayleigh scattering-based distributed fiber sensors.
- Advanced devices & instrumentation. 2021;2021.
- [45] Tan X, Abu-Obeidah A, Bao Y, Nassif H, Nasreddine W. Measurement and visualization of
- strains and cracks in CFRP post-tensioned fiber reinforced concrete beams using distributed fiber
- optic sensors. Automation in Construction. 2021;124:103604.
- [46] Fan L, Bao YJC, Composites C. Review of fiber optic sensors for corrosion monitoring in

- 693 reinforced concrete. 2021;120:104029.
- 694 [47] Froggatt M, Moore J. High-spatial-resolution distributed strain measurement in optical fiber
- 695 with Rayleigh scatter. Applied optics. 1998;37(10):1735-40.
- 696 [48] Gifford DK, Kreger ST, Sang AK, Froggatt ME, Duncan RG, Wolfe MS, et al., editors. Swept-
- 697 wavelength interferometric interrogation of fiber Rayleigh scatter for distributed sensing
- applications. Fiber Optic Sensors and Applications V; 2007: SPIE.
- 699 [49] Shojai S, Schaumann P, Brömer TJMS. Probabilistic modelling of pitting corrosion and its
- impact on stress concentrations in steel structures in the offshore wind energy. 2022;84:103232.
- 701 [50] International AG-JA. Standard guide for examination and evaluation of pitting corrosion.
- 702 2005.
- 703 [51] Ansari TQ, Luo J-L, Shi S-Q. Modeling the effect of insoluble corrosion products on pitting
- 704 corrosion kinetics of metals. NPJ Materials Degradation. 2019;3(1):1-12.
- 705 [52] Bertolini L, Elsener B, Pedeferri P, Redaelli E, Polder RB. Corrosion of steel in concrete:
- 706 prevention, diagnosis, repair: John Wiley & Sons; 2013.
- 707 [53] Melchers RE, Jeffrey RJJRE, Safety S. Probabilistic models for steel corrosion loss and pitting
- 708 of marine infrastructure. 2008;93(3):423-32.
- 709 [54] Melchers REJCS. Bi-modal trend in the long-term corrosion of aluminium alloys.
- 710 2014;82:239-47.
- 711 [55] G46-94 A. Standard guide for examination and evaluation of pitting corrosion. ASTM
- 712 International. 2005.
- 713 [56] Frankel GJJotEs. Pitting corrosion of metals: a review of the critical factors.
- 714 1998;145(6):2186.
- 715 [57] Streblow HJPM, Marcel Dekker Inc., New York, USA. Mechanisms of pitting corrosion,
- 716 Corrosion mechanism in theory in practice. 2002.
- 717 [58] Bhandari J, Khan F, Abbassi R, Garaniya V, Ojeda RJJoLPitPI. Modelling of pitting corrosion
- in marine and offshore steel structures—A technical review. 2015;37:39-62.
- 719 [59] Melchers REJC. Modeling of Marine Immersion Corrosion for Mild and Low-Alloy
- 720 SteelsPart 1: Phenomenological Model. 2003;59(04).
- 721 [60] Melchers R, Jeffrey RJEA. The critical involvement of anaerobic bacterial activity in
- modelling the corrosion behaviour of mild steel in marine environments. 2008;54(1):80-5.
- 723 [61] Deng F, Huang Y, Azarmi FJC. Corrosion behavior evaluation of coated steel using fiber
- 724 Bragg grating sensors. 2019;9(1):55.
- 725 [62] Deng F, Huang Y, Azarmi F, Wang YJC. Pitted corrosion detection of thermal sprayed metallic

- 726 coatings using fiber Bragg grating sensors. 2017;7(3):35.
- 727 [63] Melchers RE. Pitting corrosion in marine environments: a review: Department of Civil
- 728 Engineering and Surveying, University of Newcastle; 1994.
- 729 [64] Caines S, Khan F, Shirokoff JJJoLPitpI. Analysis of pitting corrosion on steel under insulation
- 730 in marine environments. 2013;26(6):1466-83.
- 731 [65] Xu S, Wang H, Li A, Wang Y, Su LJJoCSR. Effects of corrosion on surface characterization
- and mechanical properties of butt-welded joints. 2016;126:50-62.
- 733 [66] Mohd MH, Kim DK, Kim DW, Paik JKJS, structures o. A time-variant corrosion wastage
- 734 model for subsea gas pipelines. 2014;9(2):161-76.
- 735 [67] Turnbull AJPotRSAM, Physical, Sciences E. Corrosion pitting and environmentally assisted
- 736 small crack growth. 2014;470(2169):20140254.

741

- 737 [68] Zhu LK, Yan Y, Qiao LJ, Volinsky AAJCs. Stainless steel pitting and early-stage stress
- 738 corrosion cracking under ultra-low elastic load. 2013;77:360-8.
- 739 [69] International N. Standard recommended practice: preparation, installation, analysis, and
- interpretation of corrosion coupons in oilfield operations: NACE international; 2005.

Page 31